RESEARCH ARTICLE

NANO · MICRO small
www.small-journal.com

Micron-Thick Interlocked Carbon Nanotube Films with Excellent Impact Resistance via Micro-Ballistic Impact

Kailu Xiao, Pengfei Zhang, Dongmei Hu, Chenguang Huang, and Xianqian Wu**

The highest specific energy absorption (SEA) of interlocked micron-thickness carbon nanotube (IMCNT) films subjected to micro-ballistic impact is reported in this paper. The SEA of the IMCNT films ranges from 0.8 to 1.6 MJ kg^{-1}, the greatest value for micron-thickness films to date. The multiple deformation-induced dissipation channels at the nanoscale involving disorder-to-order transition, frictional sliding, and entanglement of CNT fibrils contribute to the ultra-high SEA of the IMCNT. Furthermore, an anomalous thickness dependency of the SEA is observed, that is, the SEA increases with increasing thickness, which should be ascribed to the exponential growth in nano-interface that further boosts the energy dissipation efficiency as the film thickness increases. The results indicate that the developed IMCNT overcomes the size-dependent impact resistance of traditional materials and demonstrates great potential as a bulletproof material for high-performance flexible armor.

1. Introduction

Superior impact resistance of materials is critical in meeting the increased demand for impact-protective structural design. Advanced fibre-reinforced materials with high energy-absorbing capacity have attracted significant attention in the field of impact protection.[1] The high strength of fibers and the abundant interfaces are the two main energy dissipation mechanisms during ballistic impact. Ultra-high molecular weight polyethylene (UHMWPE) fibrils,[2] Kevlar fibrils,[3] and other high-performance fibrils with amazingly specific strength and specific modulus, for example, have been intensively explored and found application in sophisticated body armor. Along with the high-performance fibrils, the assembly structures with numerous interfaces, such as cross-ply laminates,[4] woven fabrics,[5] and networked short fibrils,[6] have a considerable impact on the impact resistance of fibre-reinforced composites. During a ballistic impact, the extensive interfacial delamination and friction can dissipate efficiently the impact energy, significantly improving the impact resistance of the composites.

Carbon nanotube (CNT) fibrils,[7] as one of the promising multi-nano-interfacial materials, appear to be a capable choice for lightweight, tunable-property bulletproof armor materials.[8] Owing to multiple nano interfaces, self-supporting interlocked micron-thickness CNT (IMCNT) network films with various thicknesses can be easily harvested by densifying CNT aerogels with ethanol.[9] It shows mediocre mechanical properties under quasi-static loadings due to interfacial friction between CNT fibrils,[10] for example, elastic modulus ≈0.2–3.1 GPa, tensile strength ≈35–110 MPa.[11] However, with decreasing the thickness to hundreds of nanometer, the interlocked CNT films show excellent dynamic ballistic resistance due to the unique nanoscale network topology, which dissipates efficiently the impact energy through collapse and fracture of CNTs, frictional sliding between CNT fibrils, and entanglement of CNT bundles.[12] The 106-nm-thick CNT mats using the direct exfoliation from the thick CNT mats method demonstrated excellent specific energy absorption (SEA) ≈12 MJ kg^{-1} under 600 m s^{-1}. However, it decreased to 8 MJ kg^{-1} under the same impact velocity with increasing the thickness to 205 nm,[13] showing an obvious deterioration of the SEA when compare to that of 106-nm-thick CNT film. Generally, the SEA of films decreases significantly with increasing thickness due to the decrease of intrinsic strength at a relatively large scale resulting from the introduction of interior flaws and the negligible effects of surface energy, which is widely observed in polymer films,[14] nanocomposites film,[15] CNT fibre composite film,[8] and metallic films.[14a,16] An intriguing question, therefore, arises: if the characteristic thickness of CNT film increases to tens of microns, which is more useful for high-performance armor design, at what level is the impact resistance of IMCNT films? Does the traditional size-dependent

K. Xiao, X. Wu
Institute of Mechanics
Chinese Academy of Sciences
Beijing 100190, China
E-mail: wuxianqian@imech.ac.cn

P. Zhang, D. Hu
Key Laboratory of Multifunctional and Smart Systems
Suzhou Institute of Nano-Tech and Nano-Bionics
Chinese Academy of Sciences
Suzhou 215123, China
E-mail: dmhu2010@sinano.ac.cn

C. Huang
School of Engineering Science
University of Chinese Academy of Sciences
Beijing 100049, China

C. Huang
Hefei Institutes of Physical Science
Chinese Academy of Sciences
Hefei 230031, China

The ORCID identification number(s) for the author(s) of this article can be found under https://doi.org/10.1002/smll.202302403

DOI: 10.1002/smll.202302403

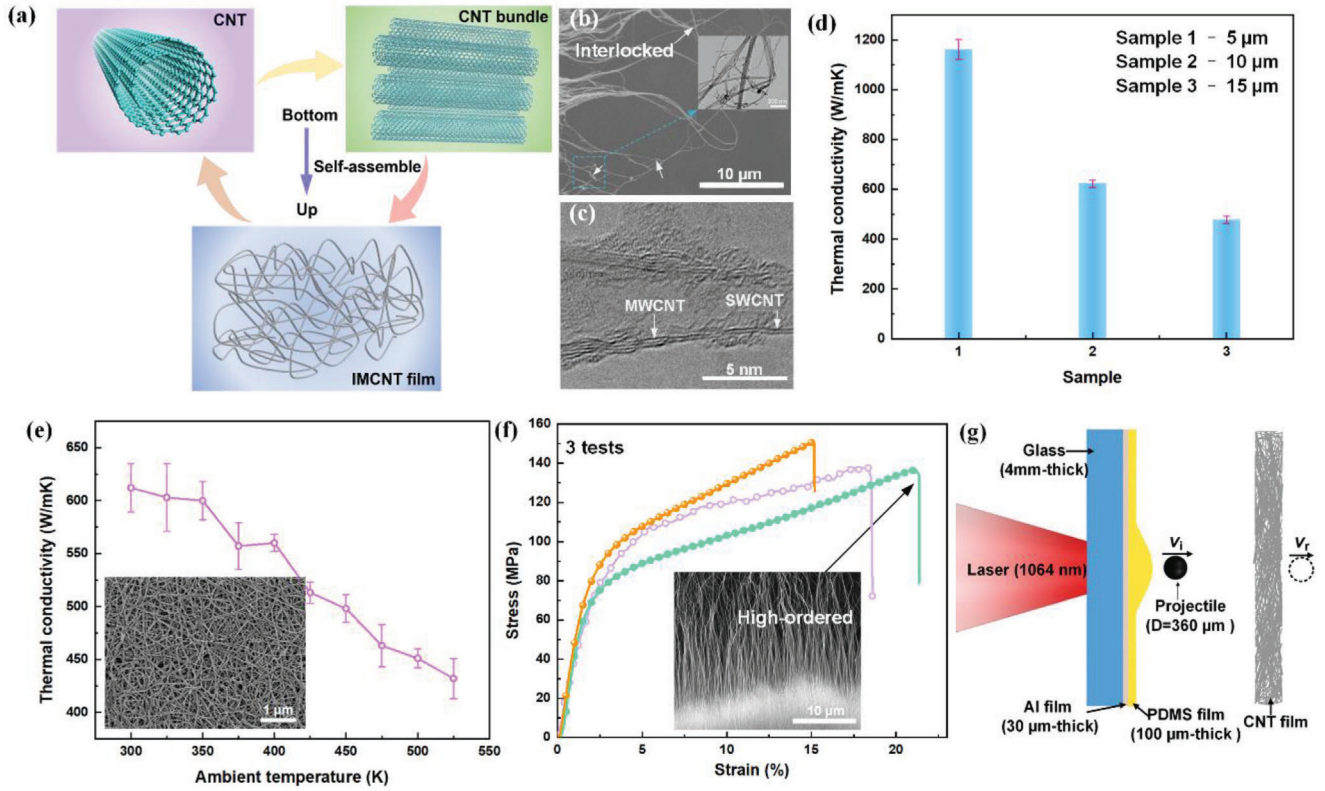

Figure 1. IMCNT film morphology, thermal and mechanical properties. a) Bottom-to-up self-assembly into the CNT aerogel. b) Scanning electron microscope (SEM) and BFTEM images of the CNT bundles, demonstrating the interlocked and entangled characteristic. c) Higher magnification of BFTEM image of IMCNT film includes dominated abundant MWCNT and a small amount of SWCNT. d) Thermal conductivity of the prepared IMCNT film with three thicknesses. e) Relationship between thermal conductivity and the ambient temperature. f) Uniaxial tensile test results of 10-μm-thick IMCNT film and the high-ordered region at the tips of the tensile fracture. g) Schematic of LIPIT setup.

impact resistance behavior of films, that is, the SEA decreases greatly with increasing thickness, still exist in IMCNT films?

Herein, the size-dependent impact resistance of IMCNT films is obtained for the first time via high-velocity micro-ballistic impact testing. The results show that the IMCNT film possesses the highest SEA over the other films with micron thickness due to the ultra-high strength of CNTs and the emergence of abundant energy dissipation channels resulting from the numerous nano-interfacial interactions during impact. Anomalous size dependence of the IMCNT film is also observed, that is, the SEA increases with increasing the thickness in the present impact velocity range, which should be ascribed to the exponential increase of interfacial density with increasing the thickness of the film. This paper provides direct proof of IMCNT films as a promising bulletproof material and suggests that the traditional size-dependent impact resistance behavior of materials needs to be revisited.

2. Results and Discussion

2.1. Characteristics of the IMCNT Film

The IMCNT films with various thicknesses were fabricated by the bottom-to-up self-assembly (Figure 1a) into the CNT aerogel, followed by densification with ethanol. The floating catalyst chemical vapor deposition (FCCVD) method was used to generate the CNT aerogels, which were collected layer by layer at the end of the corundum tube. The number of winding layers was used to control the thickness of the IMCNT films.[17] Bright-field transmission electron microscope (BFTEM) images of the IMCNT films indicate a highly porous network structure with interlocked characteristic, which consists of dominant content of multi-walled CNTs (MWCNTs) mixing with single-walled CNTs (SWCNTs) (Figure 1b,c, and Figure S1, Supporting Information).

In this paper, 5-μm-thick films, 10-μm-thick films, and 15-μm-thick films (Figure S2, Supporting Information) were prepared using 5, 10, and 15 layers of the CNT aerogels, respectively. The densities of the films were ≈0.45–0.50 g cm^{-3}. The thermal conductivity K decreases from 1160 W m^{-1} K^{-1} for the 5-μm-thick film to 478 W m^{-1} K^{-1} for the 15-μm-thick film (Figure 1d), due to the increase of inclination of CNT fibrils along the thickness direction. In addition, K decreases with the increase of environmental temperatures for the 10-μm-thick IMCNT film (Figure 1e). The elevated temperature-induced degradation of K is caused by the limitation of the phonon scattering on sample edge and grain boundaries of the IMCNT films at high temperatures, similar to crystalline solid materials.[18] Although the thermal conductivity of the IMCNT films decreases by one order of magnitude from the bottom-to-up material preparation compared to that of CNT,[19] the excellent thermal

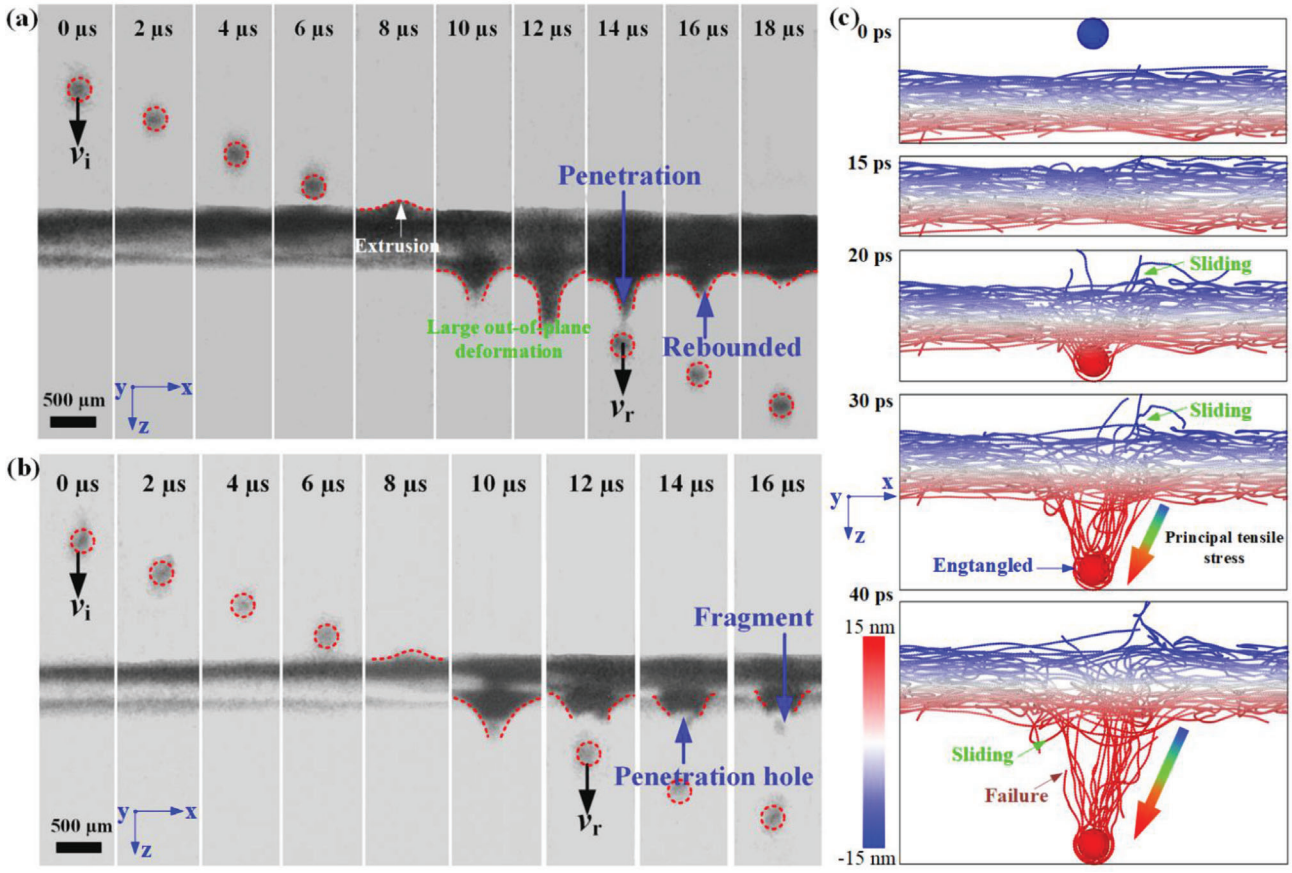

Figure 2. Impact processes obtained from experiments and simulations. a) LIPIT process of the 0.8 × 0.8 cm^2 IMCNT film at v_i = 130 ± 4.5 m s^{-1}, showing the large out-of-plane deformation and rebounded characteristic. b) LIPIT process of the IMCNT film at v_i = 175 ± 6 m s^{-1}, showing the local high deformation and fragmentation of the IMCNT film. c) Impact sequence obtained from CGMD simulations.

conductivity renders the IMCNT films a significant feature that is better than other high-performance fibrils and broadens its engineering applications.[19a,20]

The quasi-static loading tests for three 10-μm-thick IMCNT films show an in-plane elastic modulus of ≈5.8 GPa, an average failure strength of ≈140 MPa, and an average failure strain of ≈19% (Figure 1f). At high loading rates, the laser-induced projectile impact test (LIPIT) was conducted (Figure 1g) to obtain the impact resistance of the IMCNT films.[14a,16a,21] A steel spherical projectile with a diameter D = 360 μm (Figure S3, Supporting Information) was accelerated to ≈90–180 m s^{-1} and then perforated the suspended 0.8 × 0.8 cm^2 IMCNT films (Figure S4, Supporting Information). It is the highest velocity for the steel projectiles with such a 360 μm diameter for the present LIPIT system. A multi-exposure high-frame-rate camera at an interval of 2 μs is used to capture the impact process, including the transient positions of the projectile, the dynamic deformation of the IMCNT film, etc. (Figure 2a,b).

2.2. Dynamical Performance of IMCNT Film

The deformation behavior and rupture process of the IMCNT films during impact are shown in Figure 2. The profile of the projectile is marked by the red dotted circle. At low impact velocities of v_i = 130 ± 4.5 m s^{-1} (Figure 2a), there is a small extrusion at the peripheral edge of the CNT film as indicated by the red dotted curve at 8 μs. Then, the backside of the IMCNT film demonstrates large out-of-plane deformation (≈10 μm) before perforation at 10 μs and 12 μs. With the progress of the impact event, the IMCNT film is perforated eventually with a small bullet hole. Then the large-deformed film near the perforation hole begins to recover as a rubber material, exhibiting a relax-induced rebounding characteristic of the IMCNT fibrils after 14 μs as indicated by the red dotted curve. There is still residual plastic deformation after full perforation at 18 μs. During the penetration process, the re-orientation of the CNT fibrils should occur to accommodate the high strain-rate loading through friction-induced severe plasticity deformation and further dissipate the impact energy, which will be discussed in the next section. At relatively high impact velocities of v_i = 175 ± 6 m s^{-1} (Figure 2b), it shows a larger conic diameter but smaller out-of-plane deformation (≈5 μm), as indicated by the red dotted curve, which is consistent with the previous study.[22] After penetration, a broad bullet hole forms as indicated by blue arrows at 14 μs, and some fragments slide off the IMCNT film as indicated by blue arrows at 16 μs. The conic and out-of-plane deformation, the re-orientation of the CNT fibrils, and the failure of the CNT

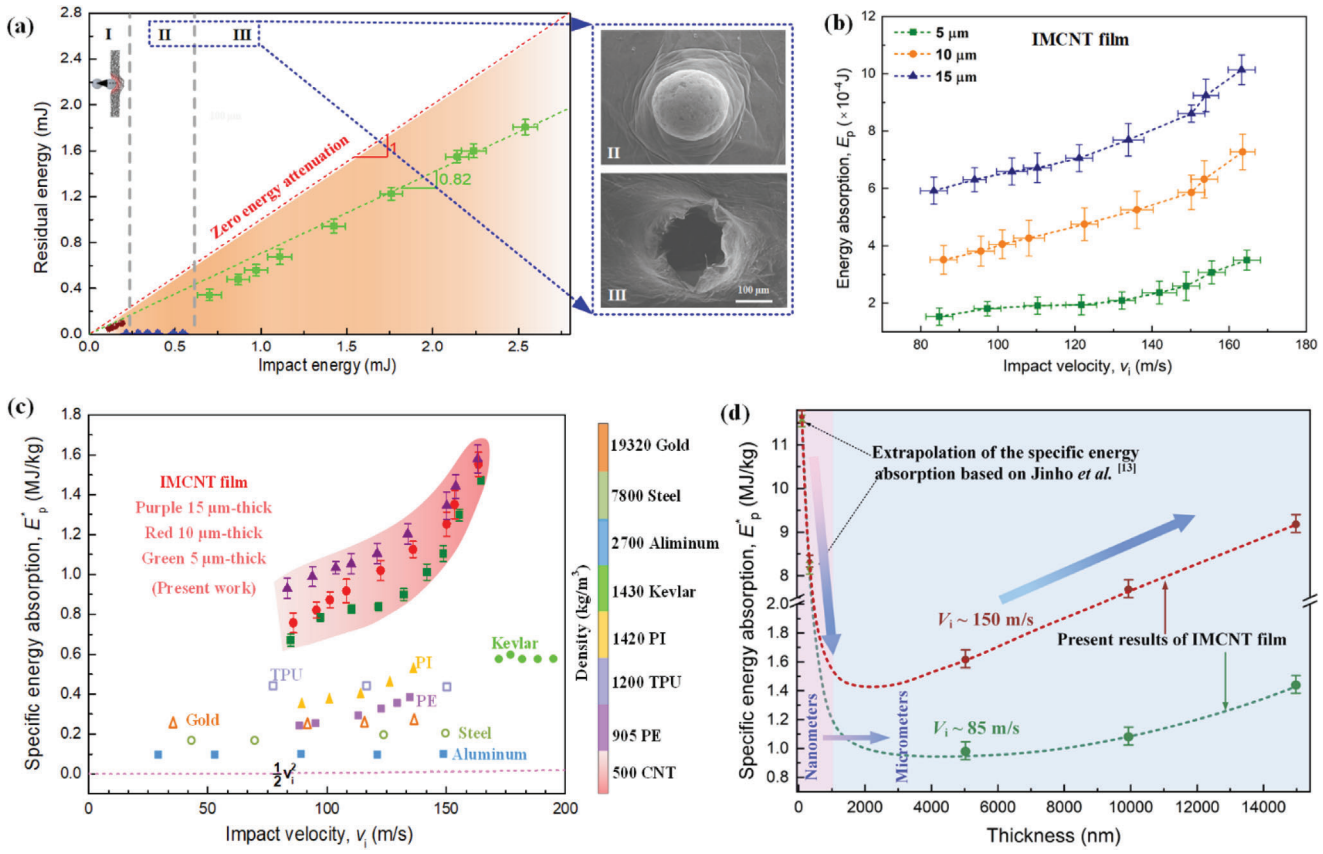

Figure 3. Energy dissipation ability of micrometers thickness IMCNT film. a) Relationship between impact energy and residual energy of 10-μm-thick IMCNT film. b) Energy absorption behavior of IMCNT film. c) SEA of IMCNT film and compared with other materials. d) A rough estimation of SEA of IMCNT films from nanometers thickness to micrometers thickness based on Jinho et al.[13]

fibrils promote the energy dissipation performance of the IMCNT films.

The impact processes simulated by the CGMD with color coding along Z-direction are shown in Figure 2c. With the chronological sequence of the impact event, the upper surface of the CNT film shows a sliding feature due to the projectile-induced friction. As the projectile reaches the back surfaces of the IMCNT network, several CNT fibrils entangle with the projectile, generating severe pull-out and substantial out-of-plane displacement. The CNT fibrils move along with the trajectory of the projectile, experiencing relatively large tensile stress and getting ordered along the tensile stress direction indicated by the colored arrows, where the blue and the red colors represent weak and strong tensile stresses, respectively. Both experiments and simulations reveal that the impact energy is successfully dissipated by friction-induced plastic deformation and the entanglement of the CNT fibrils.

According to the displacement history of the projectile captured by the high-speed camera, the v_i and v_r of the projectile are determined to analyze the impact resistance of the IMCNT films. The impact phenomenon can be divided into three characteristic regions according to the initial impact energy (Figure 3a). Taking the 10-μm-thick film as an example, in region I where the impact energy is smaller than 0.18 mJ, the projectile rebounds, and the IMCNT film undergoes elastic deformation as shown in the inset of Figure 3a. In region II where the impact energy ranges from 0.19 to 0.55 mJ, the projectile is captured eventually by the IMCNT film. The CNT fibrils in this region experience large friction-induced plasticity as evidenced by the high-reflection wrinkles, and a small fraction of the film beneath the projectile is broken. Note that the projectile didn't show obvious plastic deformation or fractures during impact. In region III where the impact energy is sufficient to perforate the IMCNT film, the residual energy increases almost linearly with increase of the initial impact energy of the projectile. A large area around the perforation hole experiences severe nominal plastic deformation, and numerous CNT fibrils are pulled out as evidenced by the fluffy periphery of the perforation hole.

During the impact, the kinetic energy loss of the projectile is $\Delta E_k = \frac{1}{2} m(v_i^2 - v_r^2)$, which is contributed by the air drag dissipated energy, E_{air}, during the flight of the micro-projectile, the air drag dissipated energy, E_f, during fast conic deformation of IMCNT film, and the energy absorbed by the IMCNT film, E_p. The energy loss due to the air drag effect can be estimated by $E_{air} = ma_{air}d_p$,[21a] where $d_p \approx 10$ mm is travel distance, m is mass of the projectile, and a_{air} is deceleration of the projectile in the air. Here, ma_{air} can also be expresses as $m\frac{dv}{dt} = -\frac{1}{2}C_D\rho_{air}Av_i^2$, where the air drag coefficient $C_D \approx 0.48$, the density of the air $\rho_{air} = 1.2$ kg m^{-3}, and A denotes the sectional area of the projectile. As a result, the E_{air} is about 2 μJ at $v_i = 82$ m/s and 9 μJ at $v_i = 175$ m/s, which is

two orders of magnitude smaller than the total energy loss of the projectile, ΔE_k. In addition, taking 10-μm-thick CNT film as an example, the E_f is about 2 μJ at $v_i = 82$ m/s and 40 μJ at $v_i = 175$ m/s (see Supporting Information), which is the same order of magnitude with E_{air}. The E_{air} and E_f are subtracted from the ΔE_k to obtain E_p as shown in Figure 3b, indicating the energy absorption ability increases with increase of impact velocity and thickness of the films. For the 15-μm-thick IMCNT film, the energy absorption increases by about 74% with increasing v_i from 82 to 175 m s^{-1}. At $v_i = 175$ m s^{-1}, the energy absorption increases by nearly 180% with increasing the thickness from 5 to 15 μm. During impact, the E_p of the IMCNT films consists of two parts, that is, the kinetic energy transferred to the impact face area A_s and the delocalized dissipated energy, E_d. Thus, $E_p = \rho A_s h \frac{v_i^2}{2} + E_d$, where ρ and h denote density and thickness of the film, respectively. Here, the SEA of the IMCNT film, $E_p^* = E_p / \rho A_s h$, which is defined as the energy absorption per unit mass of the impact region, is employed to disclose the intrinsic impact resistance of the IMCNT film. As a result, $E_p^* = \frac{v_i^2}{2} + E_d^*$, where E_d^* is specific delocalized penetration energy of the IMCNT film.

Figure 3c shows the SEA of the IMCNT films with various thicknesses under different impact velocities, indicating that the SEA increases quadratically with increasing impact velocity. It is surprising to note that the IMCNT film exhibits exceptional impact resistance ranging from 0.8 to 1.6 MJ kg^{-1} in the impact velocities ≈82–175 m s^{-1}. Compared with the 10-μm-thick polymer films (Polyethylene, PE; Polyimides, PI; Thermoplastic Polyurethane, TPU), steel foils,[23] and Kevlar fibrils,[21a] SEA of the IMCNT films outperform all these materials and increases faster with increasing impact velocity. SEA of the IMCNT films increases by ≈130%–900% when compared to the other films with micron thickness within the same range of the impact velocity, which is the highest reported value for micron-thick films to date. In addition, SEA of the IMCNT films increases with films thickness, which is counterintuitive to the traditional size-dependent impact resistance of materials. Note that the present studied thickness of IMCNT film is still smaller than the characteristic length of CNT bundles/tubes, l, that is, ≈500–1000 μm. We speculate that the SEA should decrease with increase of thicknesses when the film thickness is larger than l because the enhancement of thickness does not contribute further to the improvement of impact resistance of the IMCNT film but also introduced additional mass at the same time.

The study by Jinho et al.[13] demonstrated the high SEA of 205-nm-thick CNT mats at impact velocities of 600 to 900 m s^{-1}, and it decreases significantly with increasing thickness. However, the anomalous thickness-dependent SEA of the present IMCNT films is observed at impact velocities of 82 to 175 m s^{-1}. To compare the SEA of the CNT films with various thicknesses ranging from nanometers to present micrometers, the SEA value at 600 m s^{-1} obtained by Jinho et al.[13] is extrapolated to 150 and 85 m s^{-1} (Figure 3d) if assuming E_d^* as a constant at a given thickness. SEA of CNT films shows a sharp decrease at nanometers scale, followed by the increase at micrometers scale in the range of our present studied v_i with increasing thickness, clearly demonstrating the anomalous thickness-dependent impact resistance.

The simulated SEA values of the 8.5-nm-thick and the 25-nm-thick CNT film are 7.6 and 7.1 MJ kg^{-1} under $v_i = 600$ m s^{-1}, respectively, indicating a decreased tendency of the energy dissipation ability with thickness increasing, which agrees with the experimental observations at nanometers scale. Such a decrease of SEA with increasing thickness should be resulted from relatively easy realignment and strengthening in the peripheral region of CNT films at the nanometers scale. With increasing the thickness to micrometers, SEA increase with increasing thickness might be ascribed to the exponential increase of vdW interfaces according to CGMD simulation results, leading to the significant increase of the CNT chains that participate in energy dissipation including bending and stretching process. Here, the specific vdW energy, $\Delta E_{vdW}/M_f$, the specific stretching energy, $\Delta E_s/M_f$, and the specific bending energy, $\Delta E_b/M_f$ during impact were investigated by CGMD simulations, where ΔE_{vdW}, ΔE_s, and ΔE_b are changes of vdW energy, stretching energy, and bending energy before and after penetration (Figure S6a,b, Supporting Information), respectively, and M_f is the mass of the CNT film in the impact region. The $\Delta E_{vdW}/M_f$ of the 25-nm-thick IMCNT network is nearly 3.5 times that of the 8.5-nm-thick IMCNT network, demonstrating that thicker film dissipated more efficiently impact energy through the interactions of internal interfaces. Note that the $\Delta E_{vdW}/M_f$ is not the dominant energy dissipation method (Figure S6b, Supporting Information). It should be, however, the initial and most immediate reason for the increase of SEA with increasing thickness at micrometers scale is the exponential increase of vdW interfaces could increase significantly the $\Delta E_s/M_f$ and the $\Delta E_b/M_f$, which will be investigated in the future.

2.3. Failure Morphologies of IMCNT Film

To unveil the microstructure responses of the IMCNT film, post-mortem SEM observations are conducted after perforation. The diameter of the perforation hole is about 340 μm, which is slightly smaller than the diameter of the projectile due to the partially rebounded peripheral CNT fibrils around the perforation hole (Figure 4a). Note that the in-plane affected region is ≈450 μm. The large perforation hole indicates a plugging failure mode[24] for the IMCNT film. Besides, the residual out-of-plane deformation after perforation is marked by the red dotted circle. The enlarged red rectangular region demonstrates that there are three distinct areas of CNT fibril surrounding the penetration hole, that is, the highly oriented region (Figure 4b), the transition region (Figure 4c), and the highly disordered region (Figure 4d). In the highly oriented region (≈158 μm away from the impact center), the CNT fibrils are severely stretched and re-aligned resulting from CNT sliding during impact. The BFTEM inset of Figure 4b illustrates the highly oriented CNT fibrils near the perforation hole, indicating that there are still disordered CNT fibrils and entangled connections at the nanoscale as indicated by yellow arrows. In the transition region (≈170 μm away from the impact center), the orientation degree of the IMCNT film decreases significantly, and some CNT fibrils retain random characteristics. In the highly disordered region (>185 μm away from the impact center), the CNT fibrils keep the original disordered state and are densified due to the impact event, and no obvious

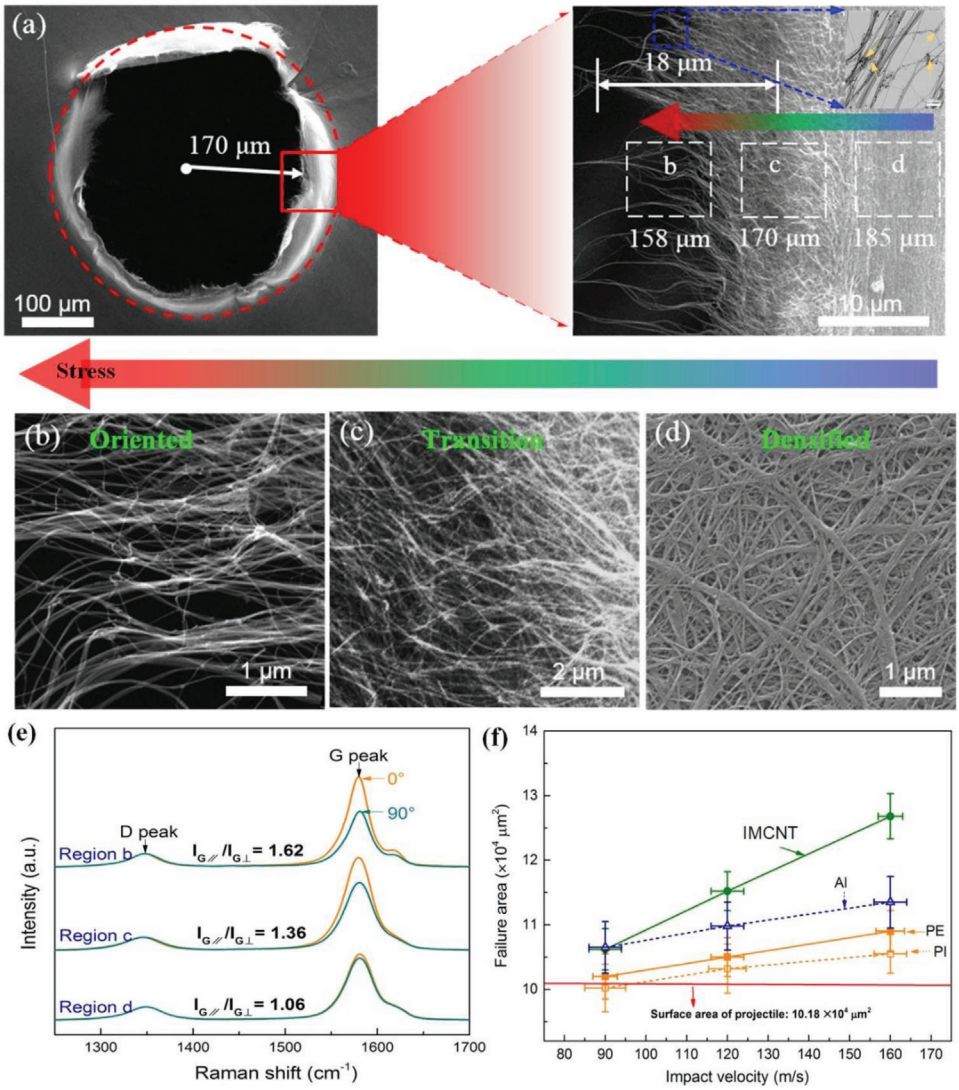

Figure 4. Post-mortem observation of the IMCNT film and characteristics. a) Damaged features of IMCNT film. b–d) Enlarged view of different regions as depicted in (a), showing the ordered characteristic, transition characteristic, and highly disordered characteristic, respectively. e) Polarized Raman spectra of different regions in (a). f) Comparison of failure area for different materials with the same thickness of 10 μm, indicating the highest delocalized energy dissipation capacity of the IMCNT film.

friction-induced plasticity is observed. The colored arrow from blue to red indicates the increase in tensile stress.

Note that the dominated energy dissipation mechanisms related to the thickness of film, impact velocity and deformation mode. At high impact velocities ($v_i > 500$ m s^{-1}), the thinner CNT film owns a higher energy dissipation ability, which was proved by Jinho et al.[13] For the thin IMCNT film under high v_i, sliding induced friction of CNT bundles, tension or bending induced deformation of CNT bundles, and the fracture of CNT bundles contributed to energy dissipation. Under low v_i, the impact kinetic energy is not enough to break a large amount of CNT bundles, so the deformation modes are mainly sliding between tubes, accompanied by entanglement and several failures of CNT fibrils. The dominant energy dissipation mode is frictional energy between interactions of IMCNT fibrils. For the present work, the deformation mode is mainly sliding and entanglement of CNT fibrils under low impact velocities, which can also be proved by the post-mortem SEM images (Figure 4b). For the present experimental method, the impact kinetic energy cannot achieve sufficient high to attain the fracture dominated energy dissipation mechanism of the IMCNT film. Other experimental technique like gas gun would be adopted to increase the impact velocity and further to study the thickness and impact velocity dependent of impact behavior of IMCNT films in the future.

The CNT alignment is also characterized by Polarized Raman spectroscopy (Figure 4e), where 0° refers to the position of the impact-induced stretching direction, and the intensities of G-band peak are recorded by $I_{G//}$ and $I_{G\perp}$ for 0° and 90°, respectively, after D-band peaks. The ratio of $I_{G//}/I_{G\perp}$ increases from 1.06 to 1.62 from region d to b, indicating the increases in the degree of alignment,[17,25] which is consistent with the impact fracture morphology. In addition, the failure areas of different materials

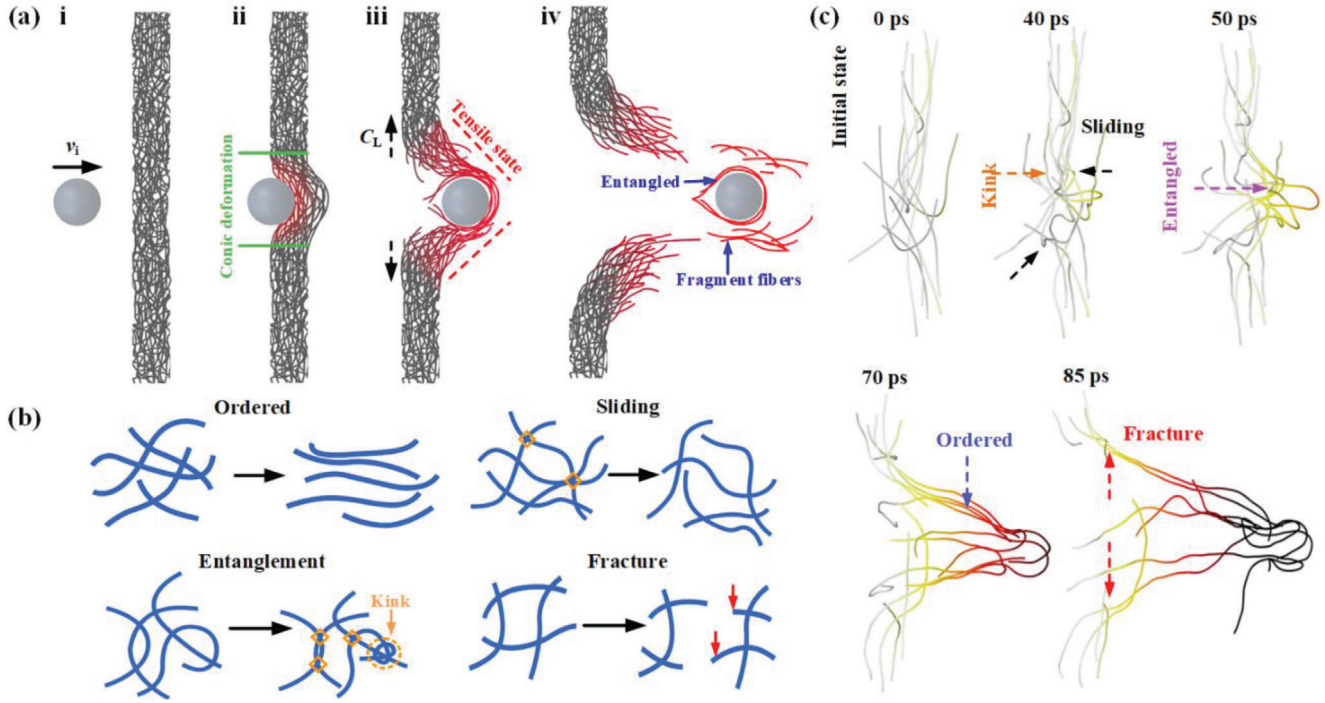

Figure 5. Schematic of the CNT fibrils evolution in the impact event. a) Schematic of impact process to illustrate the IMCNT morphology change. b) Four main energy dissipation types of CNTs during impact, including ordered, sliding, entanglement and fracture. c) CGMD simulation results demonstrate the energy dissipation channels, in which the CNT fibrils are colored by the relative displacement.

are compared (Figure 4e). The results reveal that the IMCNT film has the largest failure area when compared to the metallic films and polymer films with the same thickness of 10 μm, indicating the highest delocalized energy dissipation capacity of the IMCNT film resulting from the impact-induced sliding and entanglement of the CNT fibrils.

To illuminate the energy absorption mechanisms of the IMCNT films, the morphological evolution of the CNT fibrils and the energy dissipation channels during impact are depicted in Figure 5 according to the post-mortem observation. The central region of the IMCNT film is subjected to compression and the periphery is under shear at the beginning of impact, followed by the tension during the propagation of the longitude wave with speed C_L,[26] resulting in a conical deformation (Figure 5a-i,ii). Some CNT fibrils beneath the projectile experience dynamic stretching under high strain rates accompanied by the breaking of some CNT bundles, leading to the formation of the perforation hole eventually (Figure 5a-iii). The projectile after impact may be entangled with a few CNT fibrils and some fragmentations may detach from the IMCNT film at high impact velocities (Figure 5a-iv).

There are mainly four types of deformation modes for the CNT fibrils during impact, that is, disorder-to-order transition, relative sliding, entanglement, and fracture (Figure 5b,c). The morphologies obtained by the CGMD simulations clearly show the entanglement evolution and sliding process, eventually causing a highly entangled state of the CNT chains after impact. The fracture of CNT fibrils occurs mainly in the impact region, promoting the energy dissipation of the IMCNT film. For disorder-to-order transition, relative sliding, and entanglement surrounding the impact region, the friction of vdW interfaces dissipates efficiently the impact energy of the micro-bullet. It is worth noting that the entanglement of the CNT fibrils might cause a kink state, which will result in the obvious bending of the CNTs and is more efficient to enhance the ballistic resistance of the film. In addition to the abundant energy dissipation channels, the fast delocalization of film also contributes to the excellent impact resistance of the IMCNT films. During impact, the stress wave propagate at an extremely high speed of ≈10 km s^{-1} in each single CNT. When it arrives at the vdW interfaces, the stress waves transmit to the contacted CNTs through friction. As a result, the numerous nano-interface interaction in the IMCNT film allows the rapid delocalization of the impact energy in a large region through the synergistic action of the multiple energy dissipation channels involving stretching and bending of CNTs and friction of vdW interfaces, providing excellent impact resistance of the IMCNT film. The study suggests a promising design conception of bulletproof materials with excellent impact resistance by introducing numerous interfaces at the nanoscale.

3. Conclusions

To summarize, we fabricate micron-thick CNT films with interlocked networks. Microscopic ballistic impact experiments demonstrate that the micron-thick IMCNT films have the highest SEA values from 0.8 to 1.6 MJ kg^{-1} among the other films with micron thickness up to date. In addition, the micron-thick IMCNT films show anomalous thickness-dependent impact resistance. The deformation behavior of the IMCNT films after impact indicates that the numerous nano-interface interactions allow for rapid delocalization of the impact energy in a large

affected region, as well as synergistic action of multiple energy dissipation channels such as disorder-to-order transition, frictional sliding, entanglement, and failure of CNT fibrils, resulting in extremely high impact resistance. Our findings strongly suggest that the multiple stochastic nano-interfaces play a critical role in improving energy dissipation performance, making the micron-thick IMCNT film an ideal bulletproof material for next-generation flexible armors.

4. Experimental Section

IMCNT Film Preparation: As reported in the previous research,[27] the IMCNT networks were synthesized using the floating catalyst chemical vapor deposition (FCCVD) growth method. During the processing, ethanol was selected as a carbon source, where 1.0 wt% thiophene and 2.0 wt% ferrocene were dissolved. The solution was then transferred into the heat reaction region of the tube furnace and the temperature is about 1300 °C at a feeding rate of 0.15 mL min^{-1}. The Ar/H_2 gas mixture (volume ratio 1:1) flowed through the reactor tube at a rate of 4000 sccm. Under these conditions, the nanotubes formed continuous aerogels in the gas flow and were then blown out with the carrier gas.

The CNT aerogels were continuously wound by a rotating mandrel and densified by spraying ethanol-water solution. A multi-layered IMCNT network was prepared after evaporating the liquid, and then the prepared IMCNT film can be cut to the desired size.

Measurement of Thermal Conductivity: The "laser flash" technique (LFA447, Netzsch) and differential scanning calorimetry (DSC) were used to measure the in-plane thermal diffusivity (α) and heat capacity (C_p), respectively. Then the thermal conductivity (K) was obtained by the equation $K = \alpha \rho C_p$, where ρ is the sample density. To measure the thermal diffusivity, a 5 J energy pulse provided by the Xenon lamp was used to heat the CNT film from the bottom side, which aims to induce the temperature to rise. Then, the temperature was recorded on the top surface of the sample by a cryogenically cooled InSb IR detector. The thermal diffusivity was obtained by fitting the temperature rise attenuation.

Micro-Ballistic Test: For the setup of the LIPIT experiments, a laser pulse (10 ns pulse duration, 1064 nm wavelength) was generated by a pulsed laser system (Quanta-Ray Nd:YAG, Spectra-Physics), and was focused to a spot diameter of 2 mm for impact experiments by a 660-mm focal length lens. A 4.0-mm-thick BK7 glass was selected as a constraining layer. A 40-μm-thick aluminum film adhered to the glass surface as a laser-absorbing layer and 100-μm-thick high-elastic polydimethylsiloxane (PDMS) film was tightly attached to an aluminum film, which aimed to limit the ablation products of the aluminum film and transmit projectile kinetic energy. The 360-μm diameter spherical steel, as a projectile, was attached to the PDMS film's surface. The centers of all objects were aligned to the same straight line. The expanding gas was generated by pulsed laser ablation of aluminum film, meanwhile, the PDMS film expanded to accelerate the projectile toward the sample. At the same time, a high-frame-rate camera (SIMX, Specialized Imaging), was synchronized with a pulsed laser system by a high-precision pulse/delay generator (Model 575, Berkeley Nucleonics Corporation), recorded the photographs of the moving track of the projectile every 2 μs.

Materials Characterization: The surface morphologies of IMCNT films were characterized by scanning electron microscope (SEM, S-4800, Hitachi) at 10 kV voltage. The individual CNT structures were measured by transmission electron microscope (TEM, Tecnai G2 F20 S-TWIN, FEI) at an acceleration voltage of 200 kV. The cross-section morphology of CNT films was observed by focused ion beam microscopy (FIB, Scios, FEI). The CNT alignment was investigated by Raman spectroscopy Technique (LabRam HR800, Horriba Jobin Yvon).

CGMD Numerical Model: All CGMD simulations were performed by adopting the large-scale atomic/molecular massively parallel simulator (LAMMPS).[28] A 2D periodic boundary condition was adopted in in-plane directions X and Y. Each CNT chain contains 100 beads corresponding to the (8, 8)/(12, 12) multi-walled CNTs (MWCNTs) full-atom model owing length of 100 nm. Two different thickness IMCNT networks, that is., 8.5 and 25 nm, were established to investigate the effects of vdW energy change on the energy dissipation capability of IMCNT film. To investigate the ballistic resistance ability of a CNT film, a spherical projectile was constructed based on the diamond lattice, with a diameter of 16 nm. The diamond projectile was considered a rigid body because obvious deformation or fracture of the projectile in the experiments were not observed. This system was first equilibrated by the Langevin thermostat before mechanical loading, and the thermostat at 300 K was maintained for 1 μs to ensure the total energy converges below 0.1%. The mass density converges at 0.28 g cm^{-3}. The projectile was placed in the center of the CNT model and far away enough to avoid the interaction force in the system-equilibrated process. After equilibration, the projectile was released with an initial velocity to impact the CNT film.

Statistical Analysis: Each measured thickness of the IMCNT film was the average of seven measurements. Each V_i in LIPIT was used four times to calculate E_p^*. Error bars of experimental data were presented as mean ± standard deviation, and Microsoft Excel (Microsoft, Redmond, WA, USA) was used to calculate the error of each experiment.

Supporting Information

Supporting Information is available from the Wiley Online Library or from the author.

Acknowledgements

This work was supported by the National Natural Science Foundation of China (Grant Nos. 12272391 and 12232020), the Youth Innovation Promotion Association, CAS (D. Hu).

Conflict of Interest

The authors declare no conflict of interest.

Data Availability Statement

The data that support the findings of this study are available from the corresponding author upon reasonable request.

Keywords

dynamical performance, energy dissipation, failure morphologies, interlocked micron-thickness carbon nanotubes, size-dependent impact resistance

Received: March 21, 2023
Revised: May 1, 2023
Published online: May 21, 2023

[1] a) Shaktivesh, N. S. Nair, C. Kumar, N. K. Naik, *Mater. Des.* **2013**, *51*, 833; b) D. Varas, J. A. Artero-Guerrero, J. Pernas-Sanchez, J. Lopez-Puente, *Compos. Struct.* **2013**, *95*, 623.

[2] a) S. Arora, A. Majumdar, B., S. Butola, *J. Compos. Mater.* **2020**, *54*, 4387; b) Z. D. Sha, Q. Wan, Q. X. Pei, S. S. Quek, Z. S. Liu, Y. W. Zhang, V. B. Shenoy, *Sci. Rep.* **2014**, *4*, 7437.

[3] a) B. Sanborn, T. Weerasooriya, *Int. J. Impact Eng.* **2014**, *71*, 50; b) S. Sockalingam, S. C. Chowdhury, J. W. Gillespie, M. Keefe, *Text. Res. J.* **2016**, *87*, 984.

[4] M. R. O'Masta, D. H. Crayton, V. S. Deshpande, H. N. G. Wadley, *Int. J. Impact Eng.* **2015**, *86*, 249.
[5] A. R. Othman, M. H. Hassan, *Mater. Des.* **2013**, *44*, 407.
[6] H. Anuar, S. H. Ahmad, R. Rasid, A. Ahmad, W. N. W. Busu, *J. Appl. Polym. Sci.* **2010**, *107*, 4043.
[7] T. Inoue, I. Gunjishima, A. Okamoto, *Carbon* **2007**, *45*, 2164.
[8] J. Cai, C. Griesbach, R. Thevamaran, *ACS Nano* **2021**, *15*, 19945.
[9] a) L. J. Hall, V. R. Coluci, D. S. Galvao, M. E. Kozlov, M. Zhang, S. O. Dantas, R. H. Baughman, *Science* **2008**, *320*, 504; b) S. Iijima, *Nature* **1991**, *354*, 56; c) S. Qu, X. Jiang, Q. Li, L. Gao, G. Zhou, D. Zhang, W. Gong, W. Lu, *Carbon* **2019**, *149*, 117; d) A. Thess, R. Lee, P. Nikolaev, H. Dai, P. Petit, J. Robert, C. Xu, Y. H. Lee, S. G. Kim, A. G. Rinzler, *Science* **1996**, *273*, 483; e) S. Wang, E. Gao, Z. Xu, *Carbon* **2019**, *146*, 139; f) M. Zhang, S. Fang, A. A. Zakhidov, S. B. Lee, A. E. Aliev, C. D. Williams, K. R. Atkinson, R. H. Baughman, *Science* **2005**, *309*, 1215; g) Y. Zhang, L. Zheng, G. Sun, Z. Zhan, K. Liao, *Carbon* **2012**, *50*, 2887; h) L. Hu, D. S. Hecht, G. Grüner, *Chem. Rev.* **2010**, *110*, 5790.
[10] D. Hu, Y. Xing, M. Chen, B. Gu, B. Sun, Q. Li, *Compos. Sci. Technol.* **2017**, *141*, 137.
[11] a) S. W. Cranford, M. J. Buehler, *Nanotechnology* **2010**, *21*, 265706; b) L. Zhang, G. Zhang, C. Liu, S. Fan, *Nano Lett.* **2012**, *12*, 4848.
[12] a) K. Mylvaganam, L. C. Zhang, *Appl. Phys. Lett.* **2006**, *89*, 123127; b) K. Mylvaganam, L. C. Zhang, *Nanotechnology* **2007**, *18*, 475701; c) P. Wang, X. Zhang, R. V. Hansen, G. Sun, H. Zhang, L. Zheng, T. X. Yu, G. Lu, J. Yang, *Carbon* **2016**, *102*, 18; d) W. Xie, R. Zhang, R. J. Headrick, L. W. Taylor, S. Kooi, M. Pasquali, S. Müftü, J.-H. Lee, *Nano Lett.* **2019**, *19*, 3519.
[13] J. Hyon, O. Lawal, R. Thevamaran, Y. E. Song, E. L. Thomas, *Adv. Sci.* **2021**, *8*, 2003142.
[14] a) J. Cai, R. Thevamaran, *Nano Lett.* **2020**, *20*, 5632; b) J. Hyon, O. Lawal, O. Fried, R. Thevamaran, S. Yazdi, M. Zhou, D. Veysset, S. E. Kooi, Y. Jiao, M.-S. Hsiao, J. Streit, R. A. Vaia, E. L. Thomas, *Mater. Today* **2018**, *21*, 817.
[15] W. Xie, S. Tadepalli, S. H. Park, A. Kazemi-Moridani, Q. Jiang, S. Singamaneni, J.-H. Lee, *Nano Lett.* **2018**, *18*, 987.
[16] a) J. Hyon, M. Gonzales, J. K. Streit, O. Fried, O. Lawal, Y. Jiao, L. F. Drummy, E. L. Thomas, R. A. Vaia, *ACS Nano* **2021**, *15*, 2439; b) Y. Deng, W. Zhang, Z. Cao, *Mater. Des.* **2012**, *41*, 266; c) J. L. Dong, X. Song, Z. J. Wang, K. L. Xiao, Y. H. Liu, G. Wilde, X. Q. Wu, M. Q. Jiang, *Extreme Mech. Lett.* **2021**, *44*, 101258.
[17] Q. Liu, M. Li, Y. Gu, Y. Zhang, S. Wang, Q. Li, Z. Zhang, *Nanoscale* **2014**, *6*, 4338.
[18] A. A. Balandin, *Nat. Mater.* **2011**, *10*, 569.
[19] a) X. Zhang, W. Lu, G. Zhou, Q. Li, *Adv. Mater.* **2020**, *32*, 1902028; b) N. Mingo, D. Broido, *Phys. Rev. Lett.* **2005**, *95*, 096105.
[20] a) D. Hu, W. Gong, J. Di, D. Li, R. Li, W. Lu, B. Gu, B. Sun, Q. Li, *Carbon* **2017**, *118*, 659; b) H. Chen, M. Chen, J. Di, G. Xu, H. Li, Q. Li, *J. Phys. Chem. C* **2012**, *116*, 3903.
[21] a) J. H. Lee, P. E. Loya, J. Lou, E. L. Thomas, *Science* **2014**, *346*, 1092; b) J.-H. Lee, D. Veysset, J. P. Singer, M. Retsch, G. Saini, T. Pezeril, K. A. Nelson, E. L. Thomas, *Nat. Commun.* **2012**, *3*, 1164; c) K. Xiao, X. Wu, X. Song, J. Yuan, W. Bai, C. Wu, C. Huang, *Sci. Rep.* **2021**, *11*, 782; d) W. Xie, J.-H. Lee, *Macromolecules* **2020**, *53*, 1701; e) K. Xiao, W. Jin, H. Liu, C. Huang, Y. Li, X. Wu, *Adv. Funct. Mater.* **2023**, *33*, 2212361; f) Z. P. Gu, Y. J. Cheng, K. L. Xiao, K. Li, X. Q. Wu, Q. M. Li, C. G. Huang, *Int. J. Mech. Sci.* **2022**, *223*, 107289.
[22] K. Xiao, X. Lei, Y. Chen, Q. An, D. Hu, C. Wang, X. Wu, C. Huang, *Carbon* **2021**, *175*, 478.
[23] J. Dean, C. S. Dunleavy, P. M. Brown, T. W. Clyne, *Int. J. Impact Eng.* **2009**, *36*, 1250.
[24] A. Shahkarami, E. Cepus, R. Vaziri, A. Poursartip, in *Lightweight Ballistic Composites*, (Ed: A. Bhatnagar), Woodhead Publishing, Sawston, UK, **2006**.
[25] Q. Liu, L. Min, Z. Wang, Y. Gu, Z. Zhang, *Composites, Part A* **2013**, *55*, 102.
[26] K. Xiao, Q. Yin, X. Wu, C. Huang, *Nano Mater. Science* **2022**, *4*, 383.
[27] Q. Liu, M. Li, Y. Gu, S. Wang, Y. Zhang, Q. Li, L. Gao, Z. Zhang, *Carbon* **2015**, *86*, 46.
[28] S. Plimpton, *J. Comput. Phys.* **1995**, *117*, 1.